Spatiotemporal coherence of non-equilibrium multimode photon condensates

2016 New J. Phys. 18 103012

(http://iopscience.iop.org/1367-2630/18/10/103012)

New Journal of Physics
The open access journal at the forefront of physics

Deutsche Physikalische Gesellschaft DPG
IOP Institute of Physics

Published in partnership with: Deutsche Physikalische Gesellschaft and the Institute of Physics

OPEN ACCESS

RECEIVED
15 June 2016

REVISED
23 August 2016

ACCEPTED FOR PUBLICATION
30 August 2016

PUBLISHED
7 October 2016

PAPER

Spatiotemporal coherence of non-equilibrium multimode photon condensates

Jakov Marelic, Lydia F Zajiczek[1], Henry J Hesten, Kon H Leung, Edward Y X Ong, Florian Mintert and Robert A Nyman

Physics Department, Blackett Laboratory, Imperial College London, Prince Consort Road, SW7 2AZ, UK
[1] Present address: National Physical Laboratory, Hampton Road, Teddington, Middlesex TW11 0LW, UK.

E-mail: r.nyman@imperial.ac.uk

Keywords: Bose–Einstein condensation, microcavity, light–matter interactions, fluorescent dye, non-equilibrium

Abstract

We report on the observation of quantum coherence of Bose–Einstein condensed photons in an optically pumped, dye-filled microcavity. We find that coherence is long-range in space and time above condensation threshold, but short-range below threshold, compatible with thermal-equilibrium theory. Far above threshold, the condensate is no longer at thermal equilibrium and is fragmented over non-degenerate, spatially overlapping modes. A microscopic theory including cavity loss, molecular structure and relaxation shows that this multimode condensation is similar to multimode lasing induced by imperfect gain clamping.

1. Introduction

Quantum condensation and coherence are intimately linked for ensembles of identical particles. Condensation, defined by a macroscopically large fraction of all particles being in a single state (usually the ground state [1, 2]), is typically associated with coherence as seen in the first-order correlation function, which is proportional to the visibility of fringes of an interference measurement [3].

While observation of thermal equilibrium and macroscopic occupancy of the ground state are sometimes considered sufficient proof of Bose–Einstein condensation (BEC), the enhancement of coherence brought by BEC means that interferometry is one of the most urgent measurements to be made with a condensate [4, 5]. Where thermal equilibrium is not completely reached, coherence is the defining characteristic of non-BEC quantum condensation, e.g for semiconductor exciton-polaritons [6–9] and organic polaritons [10, 11]. In non-ideal Bose gases, such as ultracold atoms, interactions tend to reduce but not destroy the coherence [12–14].

The long range coherence behaviour of two-dimensional (2D) microcavity condensates is currently an open question. The coherence of interacting, equilibrium 2D Bose gases decays with a power law at large distances. The exponent is no greater than 1/4, which is reached at the threshold for the Berezinskii–Kosterlitz–Thouless transition [15]. It is known that the equation of motion for the local phase of a non-equilibrium driven-dissipative 2D condensate is in the universality class of the Kardar–Parisi–Zhang (KPZ) equation [16], and non-power-law decays are possible. Since the long-range coherence only shows non-equilibrium behaviour for systems which are very large compared to interaction length scales (such as the healing length), it has proven difficult to observe the true long-range behaviour, mainly due to unavoidable pumping inhomogeneities [17].

Photon condensates in dye-filled microcavities are weakly interacting [18–21], inhomogeneous [22, 23], dissipative Bose gases close to thermal equilibrium at room temperature [24–28]. It is worth noting that the physical system has some similarities to a dye laser, with the decisive difference being that lasing is necessarily a non-equilibrium effect whereas photons can also undergo BEC in thermal equilibrium. Consequently BEC implies macroscopic occupation of the ground state independently of the loss and gain properties, whereas a laser is characterised by a large occupation of exactly the mode that has the most gain [29].

Unique among physical realisations of BEC, in dye-microcavity photon BEC the particles thermalise only with a bath and not directly among themselves. This implies that the establishment of phase coherence in the

condensation process is effectively mediated via indirect interactions (such as stimulated emission) through the dye, i.e. a system whose fast relaxation renders all mediated interaction *incoherent*. Nevertheless, spontaneous selection of a condensate phase has recently been observed in the time domain [30]. Given the extremely weak interactions and substantial driving and dissipation required for the creation of a large condensate, little is known about the expected long-range behaviour of spatial coherence.

Condensates with macroscopic occupation of two or more states without phase relation are called fragmented [31]. Whereas strong, attractive interactions favour fragmentation, repulsive interactions stabilise a single condensate mode [2, 32, 33]. Fragmentation has been observed using ultracold atoms in multiple spin states [34], or separated spatial modes [35, 36]. Fragmented, dissipative condensates with spatially separated states have been seen in polaritons in semiconductors [37, 38] and in organic solids [39]. It has been proposed that for driven, dissipative bosonic systems, multimode condensation is a general non-equilibrium phenomenon [40], when the driving rates exceed the dissipation rates (such as loss, thermal equilibration or spatial re-distribution).

Far below threshold pump power, $P_{\rm th}$, the coherence time T and length L of the thermalised light are expected to be of order $h/k_B\Theta \simeq 0.15$ ps and $\lambda_{dB} = \sqrt{h\lambda_0 c \,/\, 2\pi k_B \Theta n_L^2} \simeq 1.5\ \mu$m where $\lambda_0 \simeq 590$ nm is the wavelength of the lowest-energy cavity mode, $\Theta = 300$ K the temperature, c the speed of light in free space, and n_L the refractive index of the solvent filling the cavity [41–43]. The coherence time is predicted to be much greater above threshold than below [28, 43], increasing further as the number of particles in the condensate increases, and above threshold the coherence length is expected to be at least as large as the whole condensate [44]. Multimode condensation may occur but its effect on coherence is not predicted [23].

In this manuscript we present measurements of the coherence properties of thermalised photons with both time delays and position shifts between the two arms of an interferometer. We describe how the controls and outputs of our imaging interferometer correspond to the underlying first-order correlation function, $g^{(1)}(\mathbf{r}, \mathbf{r}', \tau)$, as a function of positions $\mathbf{r}$ and $\mathbf{r}'$ and time delay τ. We characterise the coherence time and length of the photon condensate as a function of pump power. Below and just above threshold, the measurements are compatible with thermal equilibrium theory neglecting dissipation. Far above threshold, the condensate fragments into multiple, spatially distinct but overlapping, non-degenerate modes accompanied by a decrease of both spatial and temporal coherence. We explain the multimode condensation with a microscopic non-equilibrium model, and argue that the phenomenon is similar to gain saturation in lasers.

2. Experimental system

Our experiment starts by pumping a fluorescent dye in a plano-concave, 250 mm radius of curvature, high-finesse microcavity [22, 25] in quasi-continuous conditions. We use the 8th longitudinal mode of the cavity with a cutoff wavelength (corresponding to the lowest-energy cavity mode) of 590 nm. The pump spot is elliptical with an aspect ratio near unity and a minor axis of typically 50–60 μm diameter. These parameters are known to produce near thermal-equilibrium conditions [23]. The pump pulses last 500 ns, which is much longer than any thermalisation (about 300 ps) or cavity loss (about 1 ns) time scale in the system. The pulse repetition rate is varied so that the product of pump power and repetition rate is kept constant to maintain acceptable signal-to-noise over a very large range of pump powers, while avoiding a large dye triplet population. Images are typically integrated over 50–2000 ms (compared to 0.5–10 kHz pulse repetition rates).

The cavity photoluminescence is imaged to infinity, then split. Half is split again and imaged onto an auxiliary camera and a spectrometer whose spectral resolution, about 0.2 nm, is insufficient to resolve the bare cavity modes which are separated by 0.05 nm. The other half is sent to an imaging Mach–Zehnder interferometer, as shown in figure 1. Each of the two arms of the interferometer has a delay line: one controlled by a piezo for the fine motion to scan over a fringe, the other controlled by a motor for coarse motion. The horizontal axis, x, of the last adjustable mirror in one arm is controlled by a motor, whose motion is converted to a shift in position of the image at the camera. Both outputs of the interferometer are sent onto a camera through a single imaging optic, imaged to two separate locations on the sensor. There is a linear-polarising filter in front of the camera, which increases the visibility of fringes.

2.1. Data acquisition and analysis

The interferometer camera records a spatially resolved intensity distribution. If one arm of the interferometer is blocked, this corresponds to the intensity $I(\mathbf{r})$ emitted from the cavity, i.e. the spatial profile of the photoluminescence, where $\mathbf{r} = (x, y)$ is the position on the camera. Since pumping and detection in this experiment are quasi-continuous, all processes are stationary, but temporal resolution comes in terms of the path delay of the interferometer. The detected interferometer signal depends on $\mathbf{r}$, $\mathbf{r}'$ and τ, where $\mathbf{r}' = (x + \delta_x, y)$, where the displacement introduced by one arm of the interferometer is δ_x and τ is the temporal delay

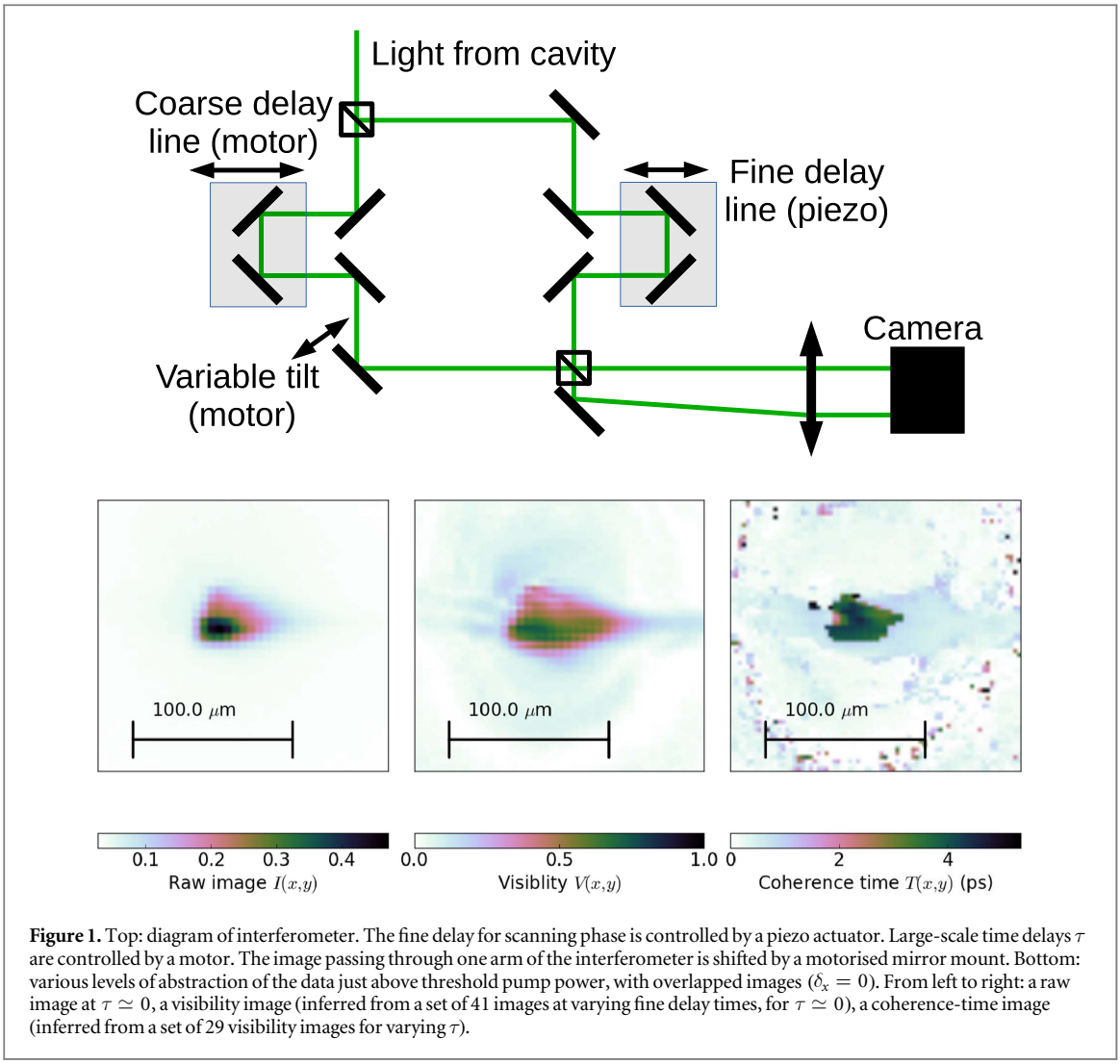

Figure 1. Top: diagram of interferometer. The fine delay for scanning phase is controlled by a piezo actuator. Large-scale time delays τ are controlled by a motor. The image passing through one arm of the interferometer is shifted by a motorised mirror mount. Bottom: various levels of abstraction of the data just above threshold pump power, with overlapped images ($\delta_x = 0$). From left to right: a raw image at $\tau \simeq 0$, a visibility image (inferred from a set of 41 images at varying fine delay times, for $\tau \simeq 0$), a coherence-time image (inferred from a set of 29 visibility images for varying τ).

corresponding to the path-length difference between the two arms of the interferometer. The Michelson visibility of fringes V is directly related to the coherence $g^{(1)}$ via the relation $V(\mathbf{r}, \mathbf{r}', \tau) = 2|g^{(1)}(\mathbf{r}, \mathbf{r}', \tau)|\sqrt{I(\mathbf{r})I(\mathbf{r}')}/[I(\mathbf{r}) + I(\mathbf{r}')]$.

To measure the visibility, we vary the voltage of the piezo controlling one of the delay lines while maintaining all other parameters fixed, so that the fine-scale delay time which we call τ_f covers about 3 periods of oscillation of the light (6 fs) at typically 41 discrete positions. At each τ_f we take an image. Coarse-scale delays, τ, up to 300 ps are achieved with the motor on the other delay line. The total delay is $\tau_f + \tau$, but we treat τ_f and τ as independent, since they vary over very different magnitudes, $|\tau_f| \ll |\tau|$. Since the microscopic description of dye-microcavity photon condensates requires no processes faster than about 100 fs [20, 27, 42, 45, 46], the coherence is expected to vary only slowly compared to the oscillations of the light.

A full set of data for measuring the spatio-temporal coherence consists of images in (x, y) for a variety of τ_f, τ and δ_x. For data sets where the pump power is varied, the exposure and gain of the camera and spectrometer are adjusted automatically to maximise dynamic range. Both output ports of the interferometer are directed to the same sensor. To allow us to align the two images in post-processing, for each set of data there is one image taken with one arm of the interferometer blocked.

All colour values from our camera are converted to monochrome by summing red and green channels. For 590 nm the sensor of our camera is equally sensitive in both red and green channels. Often 4-by-4 pixel blocks are combined to reduce computational effort in analysis. In the analysis of data sets where the control parameters of the condensate (e.g. pump power P_p) vary, an array $I(x, y, \delta_x, \tau, \tau_f, P_p)$ of values for each control parameter is constructed. The full six-dimensional data consists of as many as 25 000 images.

Extraction of the visibility over the set of fine delays is the most important processing we do on the data. Our estimator for the visibility is based on the Fourier transform of the data as a function of fine delay. It is designed to minimise the effects of sampling, amplitude and phase noise. Because we use so few fringe cycles, we sub-sample frequencies more precisely than the Nyquist criterion, improving the accuracy of the estimator.

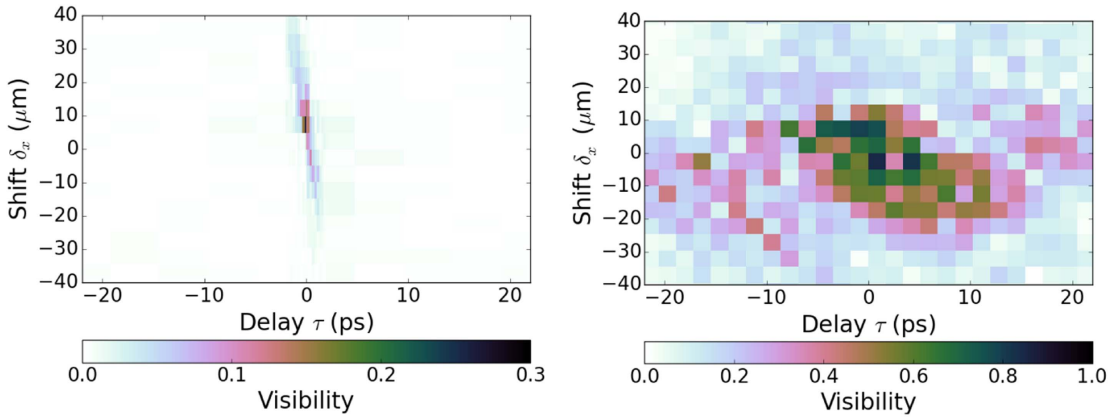

Figure 2. Visibility for a specific pixel, far below (left) and just above (right) threshold for condensation as delay and shift are varied, $V(\tau,\ \delta_x)_{x_0,y_0}$. The coherence times (lengths) are 0.2 ps (4.5 μm) for the thermal cloud and 10 ps (14 μm) for the condensate. To highlight just how low the visibility is below threshold, we have used different colour scales in the two panels.

Amplitude noise is intrinsic to the photon condensate [47], and we negate its effects by analysing the arctangent of the ratio of quadratures. Phase noise is largely due to cavity length fluctuations. We have tested the estimator against a noise model of our system and found that the estimator is unbiased except for very small (<0.05) or very large (>0.8) visibilities. Unlike the Michelson visibility criterion, our estimator is robust against amplitude noise and converts phase noise to a reduction in visibility.

For any pixel location (x, y) we can extract a characteristic coherence time T (or length L), with a fit to the visibility, usually to a Gaussian, in τ (or δ_x respectively). In figure 1 (bottom, from left to right) we see an image of the photon condensate $I(x,\ y)$, an image of the visibility $V(x,\ y)_{\delta_x=0,\tau\simeq 0}$ of the same condensate and an image of its coherence time, $T(x,\ y)_{\delta_x=0}$. $V(x,\ y)$ shows evidence of partial coherence of the thermal component surrounding the condensate despite the slightly imperfect image alignment. Visibility V and coherence $g^{(1)}$ are identically the same quantities for $\delta_x = 0$ and, experimentally δ_x is much smaller than the length scale on which intensity varies, i.e. the images are nearly overlapped. Therefore there is no discernible difference between visibility and coherence, and only V is shown in figure 1.

3. Thermal-equilibrium spatiotemporal coherence

We have measured the spatiotemporal coherence of thermalised photons far below and just above threshold, as depicted in figure 2. We choose a single pixel $x_0,\ y_0$ and measure the visibility $V(\tau,\ \delta_x)_{x_0,y_0}$ as a function of long-range delay and image shift. The differences between V and $g^{(1)}$ were not noticeable, so we have presented V. Coherence time and length are inferred from a 2D Gaussian fit to the data. Far below threshold, the length and time scales of coherence, 4.5 μm and 0.2 ps, are compatible with thermal scales taking into account finite spatial resolution (see appendix B).

The coherence is strikingly longer range in both space and time above threshold, indicative of BEC. Above threshold the measured length of the coherence, 14 μm, is comparable to the size of the condensate itself, implying that the whole condensate shares one phase, as expected. The measured coherence time of 10 ps is limited by condensate emission frequency fluctuations on timescales equal to the time between images, 200 ms. The condensate emission frequency is determined by the cavity cutoff wavelength, whose variations are dominated by the variation of the cavity length at the limits of our locking scheme, which has a bandwidth of 20 Hz and resolution equivalent to about 0.05 nm in cavity cutoff wavelength. These cavity length fluctuations relate directly to the mechanical stability of the cavity. We optimise the mechanical stability through reinforcement screws, whose precise adjustment affects the maximum coherence time we observe from one experimental data set to another. We interpret all coherence times above 2 ps as 'large' since, because of this mechanical limitation, we cannot repeatably detect longer coherence times.

3.1. Thermal equilibrium theory

The theory of correlations of a non-interacting trapped Bose gas at thermal equilibrium in the absence of dissipation is well established [48, 49], and can be extended from spatial to temporal correlations [50]. Our plano-spherical microcavity provides a symmetric, 2D, harmonic trapping potential for photons. The theory is based on a series expansion in the fugacity, where fugacity is defined as $\zeta = \exp(\mu/k_B\Theta)$, with μ the chemical

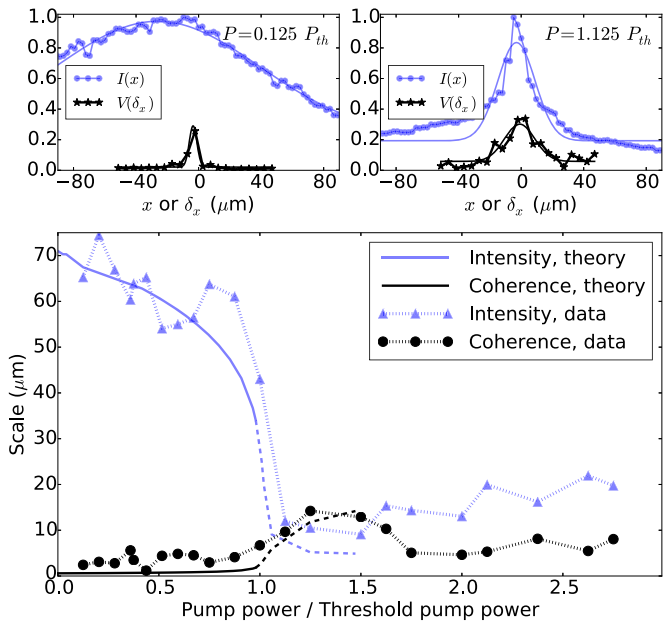

Figure 3. Coherence length as a function of pump power. Top: at pixel (x_0, y_0), for two powers P, visibility as a function of shift between images $V(\delta_x, P)_{x_0,y_0,\tau=0}$ and intensity distribution $I(x, P)_{y_0}$ are shown, together with Gaussian fits. Bottom: width of the intensity distribution and coherence length obtained from the fits. Solid lines are thermal-equilibrium theory with no adjustable parameters. Dashed lines are the same theory where it is only approximately valid.

potential and Θ the temperature, so that $\beta = 1/k_B\Theta$. The non-normalised first-order correlation function reads

$$G^{(1)}(\mathbf{r}, \mathbf{r}', t - t') = \sum_{k=1}^{\infty} \zeta^k \prod_{s=x,y} K_s^{(k)}(s, s', t, [t' - \mathrm{i}k\hbar\beta]), \tag{1}$$

where the kth term in the expansion corresponds to occupancy of up to k particles in any given mode. The function $K_s^{(k)}(s, s', t, t')$ is an unwieldy analytic function representing the propagator along the s direction, which depends on the trapping frequency (equivalent to the mode spacing), and is given in [50] equation (20). The normalised correlation function is given by its usual expression $g^{(1)}(\mathbf{r}, \mathbf{r}', t - t') = G^{(1)}(\mathbf{r}, \mathbf{r}', t - t')/\sqrt{G^{(1)}(\mathbf{r}, \mathbf{r}, 0)G^{(1)}(\mathbf{r}', \mathbf{r}', 0)}$ for stationary processes. Arbitrarily large phase-space density can be obtained for negative chemical potential, i.e. $\zeta < 1$, so the infinite series will always converge. The finite series also converges for large numbers of terms, albeit with a small positive chemical potential ($\zeta - 1 \ll 1$), for large particle numbers.

To test the convergence of the theory, we have calculated coherence length and time, and the size of the cloud of photons, for varying particle numbers and numbers of terms in the expansion. Far below threshold, the series converges as expected. Above threshold, the spatial scales of intensity and coherence converge when the series has a number of terms of the same order as the condensate population. The temporal coherence diverges above threshold, which is consistent with the non-dissipative assumptions of the theory. The calculated results qualitatively agree with exact calculations [49]. The correlation function in space matches well to a Gaussian, but the density does not due to the presence of the condensate.

While there are no adjustable parameters in the theory, the theoretical photon number does not directly correspond to the experimental pump power. Below threshold, photon number and pump power are experimentally seen and theoretically expected [28] to be linearly proportional. Likewise, far above threshold, but not so just above threshold. We can therefore directly compare our calculations to experiment only below threshold.

3.2. Variation of coherence with pump power

In figure 2 we demonstrated the coherence for two regimes, far below and just above threshold. We now present a quantitative exploration of coherence for all powers from far below to far above threshold. Visibility $V(\delta_x)$ and a cut through of the photoluminescence intensity $I(x)$ are shown in figure 3 (top), for two pump powers, one far below and one just above threshold. Since background light has not been subtracted, the Gaussian fits have a constant offset for all x. The fact that for large x the intensity sometimes dips below the fitted offset indicates that the background light is not uniform. In figure 3 (bottom), we compare experiments to the thermal equilibrium

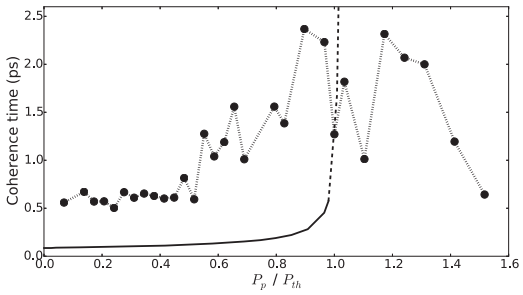

Figure 4. Coherence time as a function of pump power from Gaussian fits to $V(\tau, P)_{x_0,y_0,\delta_x=0}$. Solid line (dashed line) is the prediction assuming thermal equilibrium below threshold (and its approximate continuation above threshold).

theory without dissipation (using 999 terms in the expansion). There are no free parameters below threshold (solid lines), but the scaling of the horizontal axis is imprecise above threshold (shown as dashed lines).

Within the theory's range of validity ($P \lesssim P_{\mathrm{th}}$) there is quantitative agreement with the experiment. Far below threshold, the coherence length is much shorter than the characteristic size of photoluminescence, limited only by imaging resolution (see appendix B). With increasing power close to threshold, coherence length grows, as the width of the emitted light decreases. At even higher powers the intensity distribution broadens but the coherence length decreases to around 6 μm (approximately the harmonic oscillator length scale). In this regime, the condensate is thus only partially coherent, in contradiction to the dissipative, thermal-equilibrium prediction of [44]. Spatial coherence $V(\delta_x)$ is well described by a Gaussian. The power-law decay of correlations that is predicted for interacting 2D equilibrium condensates is observable only for displacements δ_x that are large compared to the interaction length scale (the healing length) [16]. Given the rather weak interactions in photon BECs [21], the healing length is likely to be larger than 10 μm, which is larger than the condensate. If coherence in photon BECs does follow a power-law decay, then a substantially larger condensate than currently existing will be required to observe it.

In figure 4, we show the coherence time. Far below threshold, the shortest measured coherence time is limited by spatial resolution and marginal undersampling of the data. Above threshold, an upper bound for coherence time is set by the vibrations of the cavity. At higher pump powers, coherence time decreases, suggesting partial coherence between modes, in agreement with the spatial coherence data. Even though thermal-equilibrium theory (black lines, solid below threshold, dashed above) does not describe the coherence time as accurately as spatial coherence and intensity, it captures qualitatively the increase of temporal coherence as the threshold pump power is reached.

4. Multimode non-equilibrium condensates

The change from full coherence just above threshold to partial coherence at high pump powers can be explained by the appearance of an unexpected multimode condensate phase. Figure 5 depicts the spectrum, image $I(\mathbf{r})$ and visibility image $V(\mathbf{r})$ for various pump powers above threshold. With increasing pump power the condensate peak in the spectrum breaks up into multiple peaks, i.e. the condensate splits into multiple non-degenerate modes. Figure 5 shows three peaks, but we have seen up to five distinct peaks in some experimental runs where we used reduced pump spot sizes to lower the pump threshold.

Along with this non-degenerate multimode behaviour, the condensate broadens in space and the measured visibility develops a fragmented structure. At the highest powers, the most occupied mode need not be the ground state, which is related to the imperfect alignment of a smaller pump spot for this data than for most of our other data. The spatial structures are stable over time, but change when the cavity mirrors are moved or when the dye is replaced. Because of optical imperfections (especially dye clumps but sometimes also scratches on the mirrors) the shapes of the modes of the cavity are not necessarily the Hermite–Gauss modes expected for an ideal resonator. The mode occupancies, however, are not affected by these imperfections, and it is always the lowest energy mode that shows the lowest threshold for macroscopic occupancy, i.e. BEC.

With a poorer spatial and spectral resolution, the spatial broadening could be taken as an indication of repulsive interactions. Ref [25] uses different parameters to this work (e.g. pump spot size), so it is not clear whether or not those experiments should have shown multimode condensation. Repulsive interactions strong enough to broaden the condensate by more than its initial size would also be accompanied by changes in the many-body states of the system, which would show up as a blue shift much larger than the bare-cavity mode spacing. However, since we detect no blue-shift in the spectrum apart from variations of the cavity length,

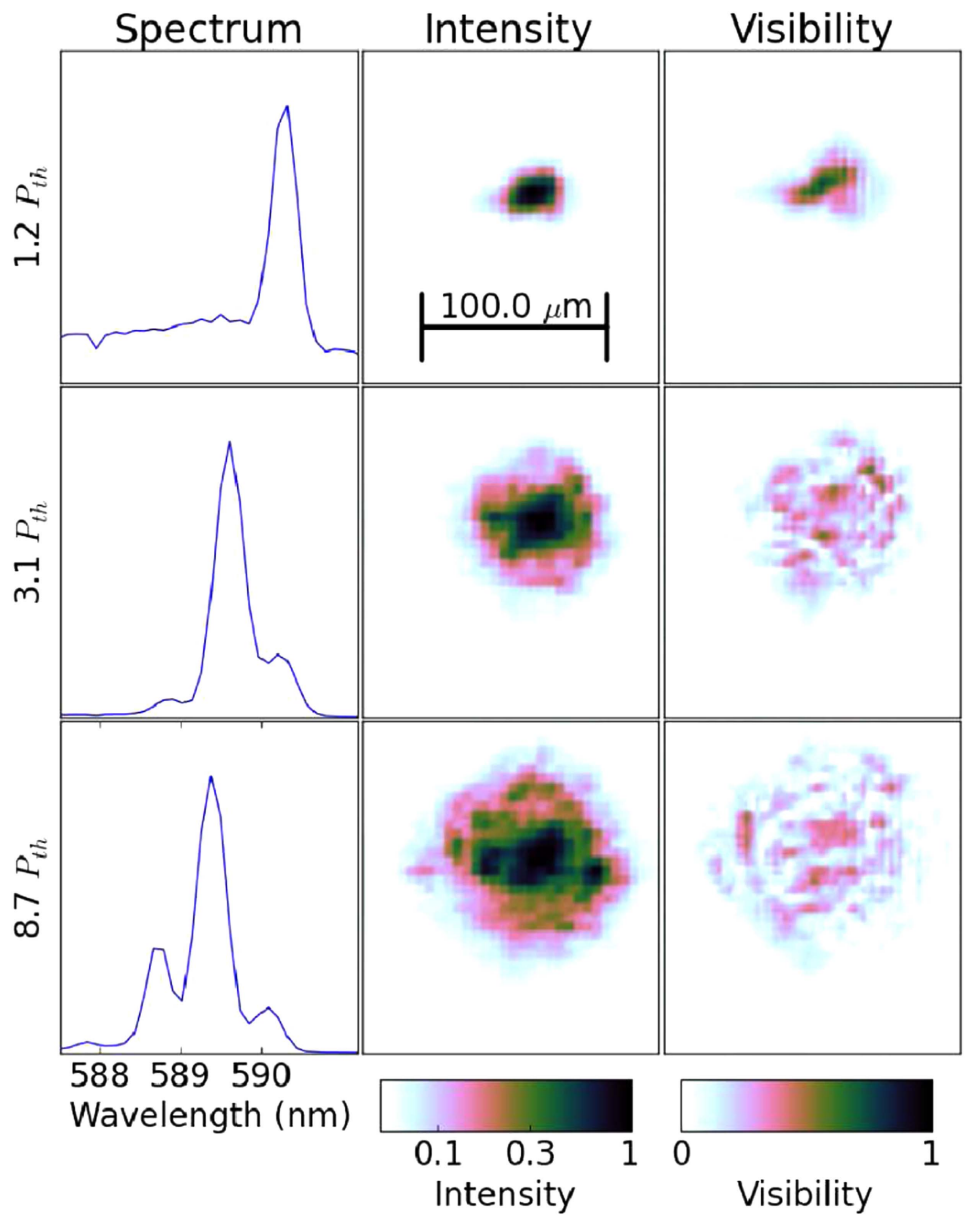

Figure 5. Normalised photoluminescence spectrum (left column), normalised image (middle column) and visibility image (right column) for various pump powers (rows, as labelled on the graph) above threshold P_{th}. The spectrum splits into multiple modes, the condensate broadens in space and the visibility image fragments at higher powers. A small pump spot (30 ± 10 μm) was used to reduce threshold pump power.

figure 5 gives clear evidence of the condensation of non-interacting photons in several modes, rather than quantum depletion reducing the condensate fraction. Since the multimode condensate is accompanied by a reduction in coherence, we conclude that the modes are incoherent, i.e. this state is a 'fragmented' condensate.

4.1. Non-equilibrium theory

Condensate fragmentation cannot be explained by thermal-equilibrium processes, which produce a single condensate, always in the lowest-energy mode. In [20] it is suggested that the multimode behaviour might occur due to imperfect clamping of the excited-state fraction of dye molecules. To explain the multimode behaviour we are thus obliged to treat the spatial dependence of dye excitation and the spatial dependence of the interaction between the dye molecules and different cavity modes. Since the thermal-equilibrium theory clearly breaks down in the multimode regime, we have implemented a non-equilibrium model [23, 27, 28]:

$$\frac{\mathrm{d}n_m}{\mathrm{d}t} = \rho_{d\mathrm{D}}\Gamma(-\delta_m)f_m(n_m + 1) - [\kappa + \rho_{d\mathrm{D}}\Gamma(\delta_m)(1 - f_m)]n_m, \tag{2}$$

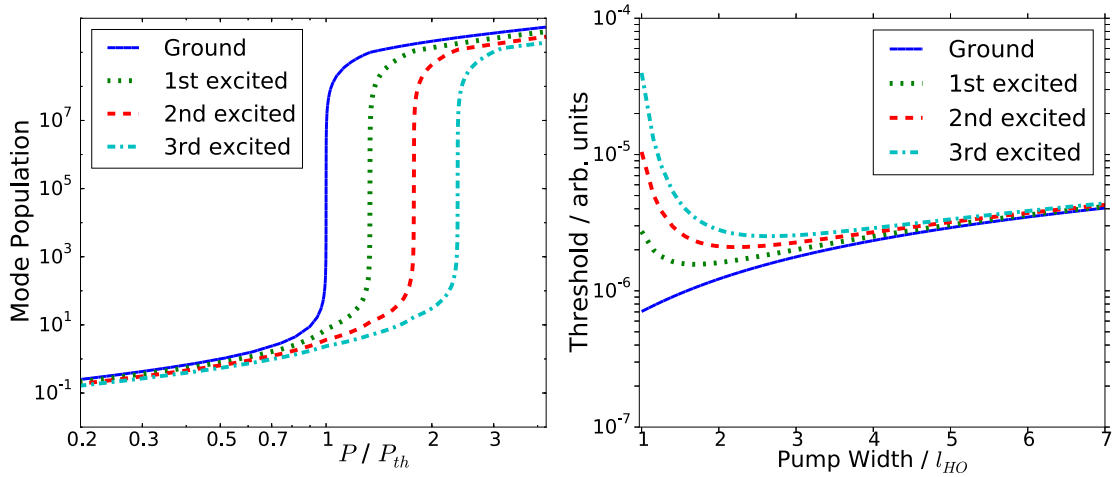

Figure 6. A microscopic model of dye molecules, cavity modes and dissipation explains the multimode behaviour. Left: for increasing pump power, first the ground state reaches threshold, then more excited modes. Right: threshold for different modes depends on the size of the pump spot, given in units of harmonic oscillator length l_{HO}. In the left panel, the pump spot size is 2.2 l_{HO}.

$$\frac{\mathrm{d}f(\mathbf{r})}{\mathrm{d}t} = -\Gamma_{\downarrow}^{\mathrm{tot}}(\{n_m\}, \mathbf{r})f(\mathbf{r}) + \Gamma_{\uparrow}^{\mathrm{tot}}(\{n_m\}, \mathbf{r})[1 - f(\mathbf{r})]. \tag{3}$$

where n_m is the occupancy of the mth mode which is detuned by δ_m from the molecular resonance (the zero-phonon line). $\Gamma(\delta)$ and $\Gamma(-\delta)$ are the absorption and emission spectra and $\rho_{d\mathrm{D}}$ the density of the dye molecules, in d dimensions. $f(\mathbf{r})$ and f_m represent the excited-state occupancy of the molecules in spatial and mode bases. The local emission and pumping rates are $\Gamma_{\uparrow}$ and $\Gamma_{\downarrow}$. Solving for the stationary solutions readily yields mode occupations which demonstrate multiple condensed modes, as in figure 5.

A crucial quantity in those equations is the absolute maximum value of light–matter coupling $\Gamma^{\max}$. The light-molecule coupling strength can be approximately derived from measured quantities, noting that the typical timescale for population variations is

$$\tau_{\mathrm{typ}} = N\Gamma_{0\mathrm{D}}(\delta) = \rho_{1\mathrm{D}}\Gamma_{1\mathrm{D}}(\delta) = \rho_{2\mathrm{D}}\Gamma_{2\mathrm{D}}(\delta), \tag{4}$$

where N is the number of molecules, $\Gamma_{d\mathrm{D}}$ and $\rho_{d\mathrm{D}}$ are the light–matter coupling and molecular density in d dimensions. In three-dimensions, the mean time between scattering events for photons moving at speed c^* from molecules at volume density $\rho_{3\mathrm{D}}$ is $\tau_{\mathrm{typ}} = 1/[\rho_{3\mathrm{D}}\, c^*\sigma(\delta)]$. Here $\sigma(\delta)$ is the scattering cross-section with its maximum $\sigma_{\max}$ found at 534 nm, the peak wavelength for absorption. Equating the timescales we find $\Gamma_{3\mathrm{D}}^{\max} = \sigma_{\max}c^* = 5.1 \times 10^{-12}\,\mathrm{m}^3\,\mathrm{s}^{-1}$. The variation of light–matter coupling with wavelength is known by interpolating experimental measurements and enforcing the Kennard–Stepanov relation [23]. In lower dimensions, the density is scaled typically by the cavity physical length and/or the harmonic oscillator length of the transverse cavity modes l_{HO}, which is 6 μm for our cavity. For computational efficiency, the model is restricted to one dimension, and only 15 modes are used, which is sufficient to ensure that the results converge, and is good enough for a qualitative comparison with experimental data. We assume a cavity decay rate of $10^9\ \mathrm{s}^{-1}$. Other parameters for the model are measured for our experiment.

In figure 6 we show the results of the model. With increasing pump power, condensation occurs first in the lowest mode, then subsequently in higher modes (left panel). When one mode reaches threshold, it locally clamps the excited state population of dye molecules, but sufficient gain remains at the edges that more modes can reach threshold. The minimum of power required to reach the multimode regime occurs when the pump spot is large enough to overlap with several spatial modes of the resonator (right panel).

The linewidth theory of [28] takes into account only the single mode into which condensation occurs. Such a truncation is only appropriate when mode filtering optics are used. Instead, here we make the approximation that dissipative processes are negligible, and the inhomogeneous broadening is responsible for the observed finite coherence. We consider the classical electric field of the light in the cavity as a coherent sum over electric fields from the many modes whose associated eigenfunction and angular frequency are known. The interferometer detectors can be used to measure the first-order correlation function remembering that only stationary processes are observed. The coherence lengths and times inferred from Gaussian fits show good qualitative agreement is in all regimes, below, near and far-above threshold.

5. Conclusions and outlook

In conclusion, we have observed first-order coherence of thermalised photons in a dye-filled microcavity, at pump powers below and above condensation threshold. Spatiotemporal correlations are longer-range for the condensed than non-condensed state, and show increases in range even below threshold, in broad agreement with thermal-equilibrium theory. Above threshold we have seen multiple condensed modes, consistent with a microscopic model that explains this fragmentation in terms of imperfect gain clamping, which is a signal of non-equilibrium, driven, dissipative processes [40].

Since there is no discernable coherence between modes, the coherence length does not always increase with pump power. This identifies a clear obstacle in the creation of large condensates, to be overcome to access the long-range coherence decay that is typical of driven-dissipative (KPZ) physics. In realising condensates that are large both in density and spatial extent, specific care needs to be taken to avoid the observed fragmentation into mutually incoherent modes. A viable route towards condensates with a size of several 10 s of microns is using cavity mirrors of large radii. To retain large particle numbers while avoiding the multimode regime, the optimal pump spot size would be matched to the condensate size.

The multimode condensation phenomenon is a result of inhomogeneous driving and dissipation. Net gain (the difference between drive and dissipation) saturates only locally, leaving gain available for modes which have not already condensed. Since those conditions are natural for trapped polaritons [9, 51] or might be engineered even for atoms [52], the observed fragmentation is by no means specific to the system at hand, but rather is expected to be observable in a variety of condensates. Since photons interact only indirectly and incoherently, but many other condensed particles have direct coherent interactions, coherence properties are a feature in which fragmented photon condensates might deviate from other condensates. In particular multimode condensation might not always result in mutually incoherent fragments as observed here, and coherence between modes is conceivable.

Acknowledgements

We thank Jonathan Keeling and Henk Stoof for inspiring discussions, and acknowledge financial support from the UK EPSRC (via fellowship EP/J017027/1 and the Controlled Quantum Dynamics CDT EP/L016524/1), and the ERC (via ODYCQUENT grant).

Appendix A. Uncertainties

There are two major sources of uncertainty in our experiments: fluctuations of threshold, and intrinsic visibility variability. The fluctuations are slightly faster than the typical time to acquire a data set, 1–5 h.

In figure A1 , we vary the pump power (in a randomised order) and measure the output light intensity averaged over a small region at the centre of the image. The pump spot was smaller than used for most of our data, to reduce threshold here. Pulse repetition rate was held constant at 500 Hz for this specific data set. Camera exposure and gain were set automatically for each power to avoid saturation, always at least 2 ms. A bi-linear least-squares fit gives that the pump source power at threshold is 260 mW (compared to around 1200 mW for

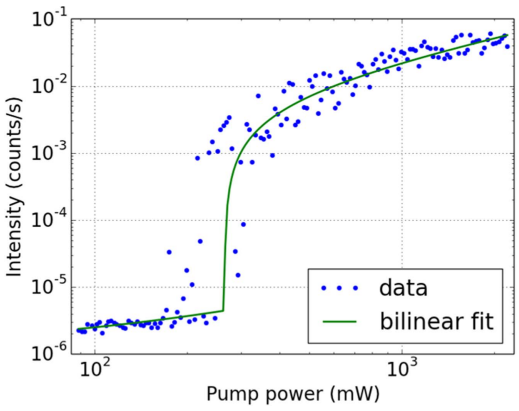

Figure A1. Threshold behaviour. A bilinear fit shows threshold around 260 mW, but many points in the range 180–250 mW show condensation. This variability in threshold limits how reliably the experiment can operate close to threshold.

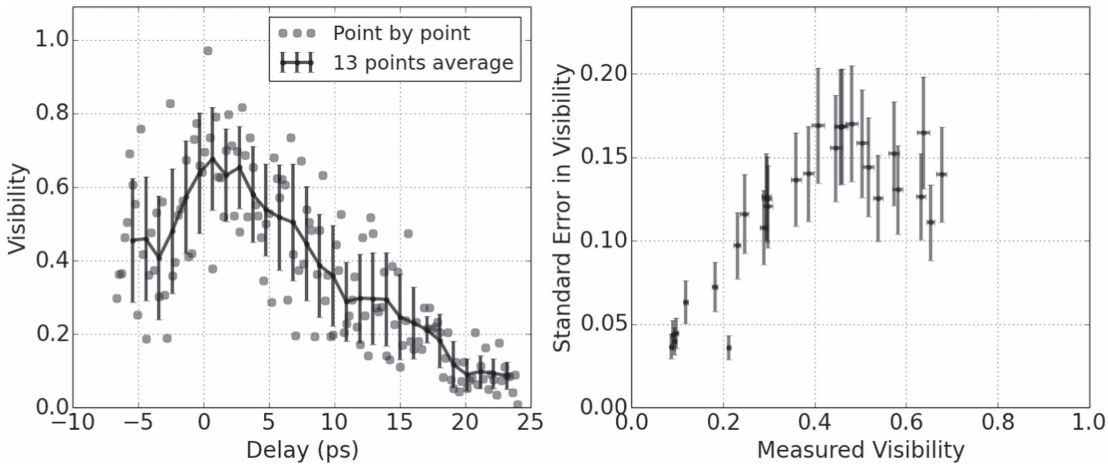

Figure A2. Limiting uncertainty in the visibility, significantly above threshold. Left: visibility variation with delay for overlapped images as a specific pixel. Grey dots are individual data points. Points with error bars are averages over 13 points centred on the marker, with error bar being the standard deviation of that sample. Right: standard deviation of visibility as a function of mean visibility. Maximum visibility inferred is 0.7. Our estimator is low-biased for the largest visibilities, and high-biased for the smallest visibility values.

most of our data). However, many points below threshold show a condensate. In the range 180–250 mW, there may be a condensate or not. This variability may be related to polymerisation of the dye, which we know occasionally forms clumps requiring cleaning of the cavity, or to pump power drifts. Alternatively, the output power from the cavity may vary during each 500 ns pump pulse due to the evolving triplet state population. Where power is varied, we reject data which are below threshold when they are expected to be above it, and vice versa. We accept only data that follow an approximately monotonic increase in output intensity as a function of pump power.

Standard-deviation errors are of limited use near threshold as there is no reason to believe that visibility measurements for a given set of parameters are drawn from a normal distribution. They are as likely to be drawn from a bimodal distribution, corresponding to below- and above-threshold behaviour. We have tried to ascertain the limiting uncertainties in visibility away from threshold, by measuring a large sample of visibilities as a function of delay above threshold: see figure A2.

By oversampling, we can build sub-samples and evaluate their standard deviations. The highest sub-sample-averaged visibility measured is about 0.7, although our estimator is low-biased for such large visibilities. The largest shot-to-shot uncertainty in visibility is 0.15. For lower average visibility, the uncertainty in the visibility is lower. For example, we can measure non-zero visibility of 0.04 with a signal-to-noise of unity in a single measurement. Our noise model produces a similar pattern only with unrealistically large phase noise. We conclude that there is intrinsic noise in the visibility which does not come from our measurement apparatus or visibility estimator.

Appendix B. Finite spatial resolution

The effect of finite imaging resolution and numerical aperture on measured interference patterns can be taken into account, by convolving the electric field at a point, $E(\mathbf{r})$ with a point-spread function $F(\mathbf{R})$:

$$\overline{E}(\mathbf{r}, t) = \int \mathrm{d}^2\mathbf{R}\, E(\mathbf{r} - \mathbf{R}, t) F(\mathbf{R}). \tag{B.1}$$

The overline indicates that finite resolution has been applied. The effect of finite numerical aperture is equivalent to applying the Fourier transform, applying a cutoff (multiplying by a top-hat function) and then inverse transforming, i.e. convolution with a cardinal sine, $\sin(x)/x$. This function can then simply be absorbed in the definition of the point-spread function, F.

The light at one output port of the interferometer is $\overline{E}_P(\mathbf{r}, \mathbf{r}', \tau) = \frac{1}{\sqrt{2}}[\overline{E}(\mathbf{r}, t) + \overline{E}(\mathbf{r}', t')]$, where as usual $\tau = t - t'$. Because we are dealing with nearly coherent light, the effects of finite resolution are applied before the interference. The other output, Q, takes a minus instead of a plus. Then the intensity is:

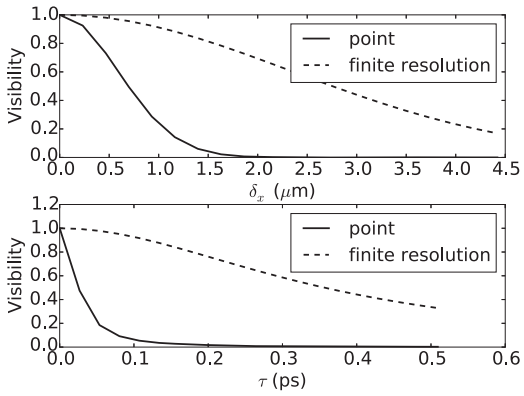

Figure B1. Calculated effect of finite imaging resolution on $g^{(1)}$ for the non-condensed photons, equivalent to $P \simeq 5 \times 10^{-3} P_{\rm th}$, using a 3 μm imaging resolution. The series expansion used 5 terms, which was sufficient for convergence so far below threshold. Top: effect on measured spatial coherence. Bottom: effect on measured temporal coherence.

$$2I_P(\mathbf{r}, \mathbf{r}', \tau) = \langle [\overline{E}^\dagger(\mathbf{r}, t) + \overline{E}^\dagger(\mathbf{r}', t')][\overline{E}(\mathbf{r}, t) + \overline{E}(\mathbf{r}', t')] \rangle$$
$$= \langle \overline{E}^\dagger(\mathbf{r}, t)\overline{E}(\mathbf{r}, t) \rangle + \langle \overline{E}^\dagger(\mathbf{r}', t')\overline{E}(\mathbf{r}', t') \rangle + 2\,\mathrm{Re}[\langle \overline{E}^\dagger(\mathbf{r}, t)\overline{E}(\mathbf{r}', t') \rangle]. \quad \text{(B.2)}$$

The first two terms are the intensities as seen with finite resolution. The last term written more explicitly, using $G^{(1)}(\mathbf{r}, \mathbf{r}', t - t') = \langle E^\dagger(\mathbf{r}, t) \rangle E(\mathbf{r}', t')$, is:

$$\langle \overline{E}^\dagger(\mathbf{r}, t)\overline{E}(\mathbf{r}', t') \rangle = \overline{G^{(1)}}(\mathbf{r}, \mathbf{r}', \tau) = \Big\langle \int \mathrm{d}^2\mathbf{R} E^\dagger(\mathbf{r} - \mathbf{R}, t) F^*(\mathbf{R}) \int \mathrm{d}^2\mathbf{R}' E(\mathbf{r}' - \mathbf{R}', t') F(\mathbf{R}') \Big\rangle$$
$$= \iint \mathrm{d}^2\mathbf{R}\mathrm{d}^2\mathbf{R}'\, F^*(\mathbf{R}) F(\mathbf{R}') G^{(1)}(\mathbf{r} - \mathbf{R}, \mathbf{r}' - \mathbf{R}', t - t'). \quad \text{(B.3)}$$

Using equation (1):

$$\overline{G^{(1)}}(\mathbf{r}, \mathbf{r}', \tau) = \sum_{k=1}^{\infty} \zeta^k \prod_{s=x,y} \iint \mathrm{d}S\, \mathrm{d}S'\, F_s^*(S) F_s(S') \times K_s^{(k)}(s - S, s' - S', t, [t' - \mathrm{i}k\hbar\beta]), \quad \text{(B.4)}$$

where we have also assumed that point-spread function is separable: $F(\mathbf{R}) = F_x(X) F_y(Y)$. This expression can be evaluated numerically, either by direct integration or via Fourier transforms The finite-resolution correlation function is normalised: $\overline{g^{(1)}}(\mathbf{r}, \mathbf{r}', \tau) = \overline{G^{(1)}}(\mathbf{r}, \mathbf{r}', \tau) \Big/ \sqrt{\overline{G^{(1)}}(\mathbf{r}, \mathbf{r}, 0)\, \overline{G^{(1)}}(\mathbf{r}', \mathbf{r}', 0)}$. The results are shown in figure B1 for a thermal cloud with pump power far below threshold ($P \simeq 5 \times 10^{-3} P_{\rm th}$). The point correlation functions show shorter range coherence than those integrated over a finite resolution (a rotationally symmetric, 3 μm Gaussian point-spread function, which is roughly the resolution of our imaging setup). Finite-resolution results are consistent with the experimental results seen at low pump powers in figures 2–4.

References

[1] Penrose O and Onsager L 1956 Bose–Einstein condensation and liquid helium *Phys. Rev.* **104** 576–84
[2] Pitaevskii L P and Stringari S 2003 *Bose–Einstein Condensation* (Oxford: Oxford University Press)
[3] Mandel L and Wolf E 1995 *Optical Coherence and Quantum Pptics* (Cambridge: Cambridge University Press)
[4] Andrews M R, Townsend C G, Miesner H-J, Durfee D S, Kurn D M and Ketterle W 1997 Observation of interference between two Bose condensates *Science* **275** 637–41
[5] Bloch I, Hänsch T W and Esslinger T 2000 Measurement of the spatial coherence of a trapped Bose gas at the phase transition *Nature* **403** 166–70
[6] Kasprzak J *et al* 2006 Bose–Einstein condensation of exciton polaritons *Nature* **443** 409–14
[7] Deng H, Press D, Götzinger S, Solomon G S, Hey R, Ploog K H and Yamamoto Y 2006 Quantum degenerate exciton-polaritons in thermal equilibrium *Phys. Rev. Lett.* **97** 146402
[8] Deng H, Solomon G S, Hey R, Ploog K H and Yamamoto Y 2007 Spatial coherence of a polariton condensate *Phys. Rev. Lett.* **99** 126403
[9] Balili R, Hartwell V, Snoke D, Pfeiffer L and West K 2007 Bose–Einstein condensation of microcavity polaritons in a trap *Science* **316** 1007–10
[10] Daskalakis K S, Maier S A, Murray R and Kéna-Cohen S 2014 Nonlinear interactions in an organic polariton condensate *Nat. Mater.* **13** 271–8
[11] Plumhof J D, Stöferle T, Mai L, Scherf U and Mahrt R F 2014 Room-temperature Bose–Einstein condensation of cavity exciton-polaritons in a polymer *Nat. Mater.* **13** 247–52
[12] Castin Y and Dalibard J 1997 Relative phase of two Bose–Einstein condensates *Phys. Rev.* A **55** 4330–7
[13] Fattori M, D'Errico C, Roati G, Zaccanti M, Jona-Lasinio M, Modugno M, Inguscio M and Modugno G 2008 Atom interferometry with a weakly interacting Bose–Einstein condensate *Phys. Rev. Lett.* **100** 080405
[14] Gustavsson M, Haller E, Mark M J, Danzl J G, Rojas-Kopeinig G and Nägerl H-C 2008 Control of interaction-induced dephasing of Bloch oscillations *Phys. Rev. Lett.* **100** 080404

[15] Nitsche W H, Young Kim N, Roumpos G, Schneider C, Kamp M, Höfling S, Forchel A and Yamamoto Y 2014 Algebraic order and the Berezinskii–Kosterlitz–Thouless transition in an exciton-polariton gas *Phys. Rev.* B **90** 205430
[16] Altman E, Sieberer L M, Chen L, Diehl S and Toner J 2015 Two-dimensional superfluidity of exciton polaritons requires strong anisotropy *Phys. Rev.* X **5** 011017
[17] Nitsche W H, Young Kim N, Roumpos G, Schneider C, Höfling S, Forchel A and Yamamoto Y 2016 Spatial correlation of two-dimensional bosonic multimode condensates *Phys. Rev.* A **93** 053622
[18] Snoke D W and Girvin S M 2013 Dynamics of phase coherence onset in Bose condensates of photons by incoherent phonon emission *J. Low Temp. Phys.* **171** 1–2
[19] Nyman R A and Szymańska M H 2014 Interactions in dye-microcavity photon condensates and the prospects for their observation *Phys. Rev.* A **89** 033844
[20] Chiocchetta A and Carusotto I 2014 Quantum langevin model for nonequilibrium condensation *Phys. Rev.* A **90** 023633
[21] van der Wurff E C I, de Leeuw A-W, Duine R A and Stoof H T C 2014 Interaction effects on number fluctuations in a Bose–Einstein condensate of light *Phys. Rev. Lett.* **113** 135301
[22] Marelic J and Nyman R A 2015 Experimental evidence for inhomogeneous pumping and energy-dependent effects in photon Bose–Einstein condensation *Phys. Rev.* A **91** 033813
[23] Keeling J and Kirton P 2016 Spatial dynamics, thermalization, and gain clamping in a photon condensate *Phys. Rev.* A **93** 013829
[24] Klaers J, Vewinger F and Weitz M 2010 Thermalization of a two-dimensional photonic gas in a ? White wall? Photon box *Nat. Phys.* **6** 512–5
[25] Klaers J, Schmitt J, Vewinger F and Weitz M 2010 Bose–Einstein condensation of photons in an optical microcavity *Nature* **468** 545–8
[26] Schmitt J, Damm T, Dung D, Vewinger F, Klaers J and Weitz M 2015 Thermalization kinetics of light: from laser dynamics to equilibrium condensation of photons *Phys. Rev.* A **92** 011602
[27] Kirton P and Keeling J 2013 Nonequilibrium model of photon condensation *Phys. Rev. Lett.* **111** 100404
[28] Kirton P and Keeling J 2015 Thermalization and breakdown of thermalization in photon condensates *Phys. Rev.* A **91** 033826
[29] Fischer B and Weill R 2012 When does single-mode lasing become a condensation phenomenon? *Opt. Express* **20** 26704–13
[30] Schmitt J, Damm T, Dung D, Wahl C, Vewinger F, Klaers J and Weitz M 2016 Spontaneous symmetry breaking and phase coherence of a photon Bose–Einstein condensate coupled to a reservoir *Phys. Rev. Lett.* **116** 033604
[31] Mueller E J, Ho T-L, Ueda M and Baym G 2006 Fragmentation of Bose–Einstein condensates *Phys. Rev.* A **74** 033612
[32] Leggett A J 2001 Bose–Einstein condensation in the alkali gases: some fundamental concepts *Rev. Mod. Phys.* **73** 307–56
[33] Nozières P 1995 *Bose–Einstein Condensation* (Cambridge: Cambridge University Press)
[34] Sarlo L D, Shao L, Corre V, Zibold T, Jacob D, Dalibard J and Gerbier F 2013 Spin fragmentation of Bose–Einstein condensates with antiferromagnetic interactions *New J. Phys.* **15** 113039
[35] Chen Y P, Hitchcock J, Dries D, Junker M, Welford C and Hulet R G 2008 Phase coherence and superfluid-insulator transition in a disordered Bose–Einstein condensate *Phys. Rev.* A **77** 033632
[36] Krinner S, Stadler D, Meineke J, Brantut J-P and Esslinger T 2015 Observation of a fragmented, strongly interacting Fermi gas *Phys. Rev. Lett.* **115** 045302
[37] Richard M, Kasprzak J, André R, Romestain R, Dang L S, Malpuech G and Kavokin A 2005 Experimental evidence for nonequilibrium Bose condensation of exciton polaritons *Phys. Rev.* B **72** 201301
[38] Cerda-Méndez E A, Krizhanovskii D N, Wouters M, Bradley R, Biermann K, Guda K, Hey R, Santos P V, Sarkar D and Skolnick M S 2010 Polariton condensation in dynamic acoustic lattices *Phys. Rev. Lett.* **105** 116402
[39] Daskalakis K S, Maier S A and Kéna-Cohen S 2015 Spatial coherence and stability in a disordered organic polariton condensate *Phys. Rev. Lett.* **115** 035301
[40] Vorberg D, Wustmann W, Ketzmerick R and Eckardt A 2013 Generalized Bose–Einstein condensation into multiple states in driven-dissipative systems *Phys. Rev. Lett.* **111** 240405
[41] Guarrera V, Würtz P, Ewerbeck A, Vogler A, Barontini G and Ott H 2011 Observation of local temporal correlations in trapped quantum gases *Phys. Rev. Lett.* **107** 160403
[42] de Leeuw A-W, Stoof H T C and Duine R A 2013 Schwinger–Keldysh theory for Bose–Einstein condensation of photons in a dye-filled optical microcavity *Phys. Rev.* A **88** 033829
[43] de Leeuw A-W, van der Wurff E C I, Duine R A and Stoof H T C 2014 Phase diffusion in a Bose–Einstein condensate of light *Phys. Rev.* A **90** 043627
[44] de Leeuw A-W, Stoof H T C and Duine R A 2014 Phase fluctuations and first-order correlation functions of dissipative Bose–Einstein condensates *Phys. Rev.* A **89** 053627
[45] Sob'yanin D N 2013 Bose–Einstein condensation of light: general theory *Phys. Rev.* E **88** 022132
[46] Klaers J, Schmitt J, Damm T, Vewinger F and Weitz M 2012 Statistical physics of Bose–Einstein-condensed light in a dye microcavity *Phys. Rev. Lett.* **108** 160403
[47] Schmitt J, Damm T, Dung D, Vewinger F, Klaers J and Weitz M 2014 Observation of grand-canonical number statistics in a photon Bose–Einstein condensate *Phys. Rev. Lett.* **112** 030401
[48] Naraschewski M and Glauber R J 1999 Spatial coherence and density correlations of trapped Bose gases *Phys. Rev.* A **59** 4595–607
[49] Barnett S M, Franke-Arnold S, Arnold A S and Baxter C 2000 Coherence length for a trapped Bose gas *J. Phys. B: At. Mol. Opt. Phys.* **33** 4177
[50] Kohnen M and Nyman R A 2015 Temporal and spatiotemporal correlation functions for trapped Bose gases *Phys. Rev.* A **91** 033612
[51] Winkler K *et al* 2016 Collective state transitions of exciton-polaritons loaded into a periodic potential *Phys. Rev.* B **93** 121303
[52] Barontini G, Labouvie R, Stubenrauch F, Vogler A, Guarrera V and Ott H 2013 Controlling the dynamics of an open many-body quantum system with localized dissipation *Phys. Rev. Lett.* **110** 035302